Astronomy & Astrophysics manuscript no. output
June 30, 2026
©ESO 2026

Resolving SLX 1744−299 and SLX 1744−300 in the hard X-ray band: Implications for their ultracompact nature

Enzo A. Saavedra[1,2], Montserrat Armas Padilla[1,2], and Teo Muñoz-Darias[1,2]

[1] Instituto de Astrofísica de Canarias (IAC), Vía Láctea s/n, La Laguna 38205, S/C de Tenerife, Spain
[2] Departamento de Astrofísica, Universidad de La Laguna, La Laguna, E-38205, S/C de Tenerife, Spain

Received; accepted

ABSTRACT

Persistent, low-luminosity low-mass X-ray binaries offer a unique opportunity to study accretion in this poorly understood regime as well as to unveil new members of the ultracompact X-ray binary (UCXB) family, which are characterised by orbital periods ($P_{\rm orb}$) shorter than $\sim$ 80 min. We report on a *NuSTAR* archival observation that, for the first time above 10 keV, spatially resolves the Galactic Centre pair SLX 1744−299 and SLX 1744−300. We find SLX 1744−300 to be slightly brighter, with a flux ratio of $\sim$ 1.15, increasing to $\sim$ 1.3 when extrapolated to 0.5–10 keV. Both the timing (root-mean-square variability) and spectral properties (well described in both cases by a thermal Comptonisation model) indicate that the systems were in the hard state. The two sources, however, display markedly different behaviour throughout the observation. SLX 1744−299 shows a gradual flux decline consistent with a decrease in the mass-accretion rate, whereas SLX 1744−300 remains steady but exhibits two short-recurrence Type-I X-ray bursts indicative of mixed H and He burning.

Combining our results with previously reported upper limits on the distance, we derived low persistent X-ray luminosities of $L_{\rm X} \lesssim 1.1 \times 10^{36}$ erg s^{-1} and $L_{\rm X} \lesssim 2.6 \times 10^{36}$ erg s^{-1} (3–78 keV) for SLX 1744−299 and SLX 1744−300, respectively. The corresponding mass-accretion rates, when compared with the critical values from the disc instability model, favour $P_{\rm orb} \lesssim 90$ min and $P_{\rm orb} \lesssim 105$–155 min. Although both limits are formally compatible with the UCXB regime, the case of SLX 1744−299 appears significantly more compelling, also considering the previously reported intermediate-duration burst.

Key words. accretion, accretion discs — stars: neutron — X-rays: binaries

1. Introduction

Low-mass X-ray binaries (LMXBs) are stellar systems in which a compact object, either a black hole or a neutron star (NS), accretes matter from a low-mass companion star ($\lesssim 1 M_\odot$; see Bahramian & Degenaar 2023, for a recent review). To date, approximately 340 such systems have been identified in our Galaxy (see e.g., Fortin et al. 2024).

Of particular interest among LMXBs are ultracompact X-ray binaries (UCXBs), which are characterised by very short orbital periods ($P_{\rm orb} \lesssim 80$ min). In these tight systems, the companion is a degenerate or semi-degenerate star that no longer burns hydrogen in its core and may consist of electron-degenerate matter (e.g. Paczynski & Sienkiewicz 1981; Rappaport et al. 1982; Verbunt & van den Heuvel 1995). Therefore, these systems serve as unique laboratories for studying accretion processes in hydrogen-poor environments (e.g. Nelemans & Jonker 2010). Additionally, UCXBs are expected to be strong sources of low-frequency gravitational waves, making them key targets for the upcoming Laser Interferometer Space Antenna (LISA) mission (e.g. Nelemans 2018; Tauris 2018; Chen et al. 2021; Amaro-Seoane et al. 2023).

Currently, there are only 20 confirmed UCXBs (i.e. with a measured orbital period shorter than 80 min) and 25 UCXB candidates (see the online version of the UltraCompCAT catalogue[1]; Armas Padilla et al. 2023). Yet, the estimated number of UCXBs expected to exist in our Galaxy is $(0.2 - 1.9) \times 10^5$ (Zhu et al. 2012; van Haaften et al. 2013). Measuring $P_{\rm orb}$ in these systems is observationally challenging. While X-ray timing techniques can be applied in systems hosting pulsars or showing eclipses or dips, most sources lack such features. In the optical, when a counterpart is detected, it is typically intrinsically faint, often requiring exposure times comparable to or longer than the orbital period. However, in the absence of a measured orbital period, indirect diagnostics can be used to identify UCXB candidates. These include signatures of the degenerate nature of the donor star, such as the presence or absence of specific emission and absorption features in the source spectra, as well as the properties of thermonuclear X-ray bursts (e.g. duration, recurrence time, and radiated energy), which provide insights into the composition of the accreted fuel. Likewise, the small size of the accretion disc in UCXBs results in lower optical-to-X-ray flux ratios than those associated with regular LMXBs, as the reprocessing region responsible for the optical emission is also reduced (for more details, see Armas Padilla et al. 2023). Last but not least, small discs can remain fully ionised when accreting at low rates, as predicted by the disc instability model (DIM; Lasota 2001), allowing UCXBs to sustain persistent accretion even at X-ray luminosities as low as $L_{\rm X} \lesssim 10^{36}$ erg s^{-1} (see, e.g., in't Zand et al. 2007). This makes persistently accreting, low-luminosity LMXBs strong UCXB candidates.

SLX 1744−299 and SLX 1744−300 are two LMXBs located ~2.7 arcmin apart and ~2.3 arcmin from the pulsar PSR J1747−2958 (known as 'the Mouse'; Skinner et al. 1990; Pavlinsky et al. 2021). Owing to their small angular separation, they were initially detected as a single X-ray source with the tele-

[1] https://research.iac.es/proyecto/compactos/UltraCompCAT

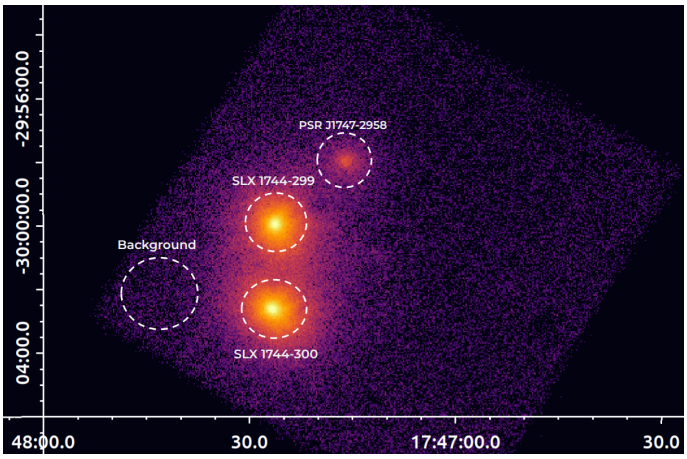


Fig. 1: *NuSTAR* FPMA module image in the 3–78 keV energy band showing the field of the LMXBs SLX 1744-299 (north) and SLX 1744-300 (south). The pulsar PSR J1747-2958 (also known as "the Mouse") is visible within the field. The dashed circular regions indicate the event and background extraction regions for each source.

scope aboard Spacelab 2 (Skinner et al. 1987, see also Kawai et al. 1988), and were only identified as two distinct objects a few years later through improved image reconstruction techniques (Skinner et al. 1990). Both LMXBs exhibit persistent fluxes of $\sim 10^{-10}$ erg cm^{-2} s^{-1} in the 2–10 keV range, with the flux of SLX 1744−299 being approximately twice that of SLX 1744−300 (Mori et al. 2005). However, long-term monitoring of the field with the *Rossi* X-ray Timing Explorer showed that the unresolved emission varies by roughly a factor of two, hinting at the possibility that either or both sources are variable (in't Zand et al. 2007). Type-I thermonuclear X-ray bursts have been observed in both systems, confirming the NS nature of their compact objects (Skinner et al. 1990; Pavlinsky et al. 1994; Mori et al. 2005; Galloway et al. 2008). In particular, SLX 1744−299 has exhibited several intermediate-duration bursts, which typically last a few minutes (Pavlinsky et al. 1994; in't Zand et al. 2007; Alizai et al. 2020). None of the bursts from either system has shown photospheric radius expansion, so only upper limits on their distances have been estimated: 7.2 ± 1.4 kpc for SLX 1744−299 and 10.3 ± 0.8 kpc for SLX 1744−300 (Chelovekov et al. 2017). These values translate into low persistent luminosities ($\lesssim 10^{36}$ erg s^{-1}) in both cases. This, together with the presence of intermediate-duration bursts, has led to the classification of SLX 1744−299 as a UCXB candidate (in't Zand et al. 2007). The nature of SLX 1744−300, on the other hand, remains largely unconstrained.

In this paper we present a detailed X-ray spectral and temporal analysis of a *NuSTAR* observation that, for the first time, resolves both systems individually in the hard X-ray band above 10 keV. This allowed us to characterise their hard X-ray spectra and further investigate their nature.

2. Data reduction and analysis

The *Nuclear Spectroscopic Telescope Array* (*NuSTAR*) observed the field on 2018 July 29 (ObsID 30401036002; Harrison et al. 2013), with an on-source exposure time of 44.2 ks over an elapsed time of 79 ks. Three sources were detected in this observation: SLX 1744−299, SLX 1744−300 and the pulsar PSR J1747-2958 (see Figure 1).

We processed the data using the *NuSTAR* Data Analysis Software (NuSTARDAS) included in the HEASOFT v6.34 package, along with calibration files from CALDB (v.20251215). The NUPIPELINE tool employed the parameters SAACALC=1, SAAMODE=OPTIMIZED, and TENTACLE=NO to filter out passages through the South Atlantic Anomaly (SAA)[2]. We also verified that no additional correction for the multi-layer insulation tear on the focal plane module A (FPMA) was required (Madsen et al. 2020). Barycentric corrections were applied using the clock correction file 20100101v178. Source events were extracted from a circular region with a radius of 50 arcsec, centred on the centroid of the counts distribution for each LMXB. For background events, we used a circular region with a radius of 70 arcsec in a source-free area in the same chip as the targets (see Figure 1).

Given the close proximity of the two sources on the sky ($\sim$ 2.7 arcmin) and the size of the extraction regions (R = 50 arcsec), we assessed the potential impact of cross-contamination due to the broad wings of the *NuSTAR* point spread function. We performed numerical simulations using a King profile, calibrated to match the in-flight full width at-half maximum (18″) and half power diameter (58″; Harrison et al. 2013; Koglin et al. 2011). We estimate cross-contamination fractions of 0.99±0.07 per cent for SLX 1744−299 and 0.76 ± 0.06 per cent for SLX 1744−300, and therefore their impact is negligible in our analysis.

Background-subtracted light curves were extracted for both FPMA and FPMB separately and then combined using the `lcmath` task from the FTOOLS package (Blackburn 1995). The extracted spectra from each module were grouped with a minimum of 30 counts per bin, allowing the use of the χ^2 statistic. In the remainder of this section, we describe the temporal and spectral analyses applied to both sources.

2.1. Temporal analysis

In order to search for potential pulsation candidates, we analysed the data from the two targets in the 0.1–10 Hz frequency range using the `HENDRICS` tool (Bachetti 2018). We used the HENACCELSEARCH module to identify optimal pulsation candidates within the specified frequency range. In addition, we derived a 90 per cent confidence upper limit on the pulsed fraction using the `HENz2vspf` tool, based on 10^4 simulations (see Cruz-Sanchez et al. 2026a,b, for more details). Finally, we generated the Leahy-normalised power density spectra using the `Stingray` software package (Huppenkothen et al. 2019) and applied the Fourier amplitude difference method to correct for dead time (Bachetti & Huppenkothen 2018). We calculated the fractional root-mean-square (rms) amplitude in the 0.1–64 Hz range following the method described by Muñoz-Darias et al. (2011, 2014). Specifically, we used data in the 3–15 keV energy band, divided into 64 s segments. We used a time resolution corresponding to a Nyquist frequency of 1000 Hz; this ensures an accurate estimate of the Poisson (white) noise level when computing the power density spectra.

2.2. Spectral analysis

We simultaneously fitted the 3–78 keV FPMA and FPMB spectra using XSPEC (v.12.14.0; Arnaud 1996), with the parameters tied between the two modules. We included a multiplicative constant factor in our models, fixing it to 1.0 for FPMA and allowing

[2] https://nustarsoc.caltech.edu/NuSTAR_Public/NuSTAROperationSite/SAA_Filtering/nulyses_reports/30401036002/nu30401036002_SAA_Report_A.pdf

it to vary freely for FPMB, to account for differences in their calibration.

We modelled the interstellar absorption using the Tübingen-Boulder model (TBabs), setting the solar abundances according to Wilms et al. (2000) and the effective cross-sections to Verner et al. (1996). We fixed the hydrogen column density ($N_{\rm H}$) to 3.3×10^{22} cm^{-2} for SLX 1744−299 and 3.7×10^{22} cm^{-2} for SLX 1744−300, as obtained by Mori et al. (2005) from *XMM-Newton* observations. Throughout this work, we assumed the upper limits on the distance of 7.2 ± 1.4 kpc (SLX 1744−299) and 10.3±0.8 kpc (SLX 1744−300) derived from the analysis of thermonuclear bursts (Chelovekov et al. 2017).

We tested various spectral models, combining up to three components, aimed at addressing the main X-ray spectral features typically observed in NS-LMXBs. For the soft, thermal emission from the accretion disc, we used a multicolour disc (MCD) model (`diskbb`; Mitsuda et al. 1984; Makishima et al. 1986). A blackbody (BB) model (`bbodyrad`) was used to account for the soft, thermal emission from the NS surface or boundary layer. For the thermally Comptonised emission from the corona, we used the `nthComp` model, setting the seed-photon geometry (`inp_Type`) to 0 for a BB geometry and 1 for an accretion disc geometry (Zdziarski et al. 1996; Życki et al. 1999). In our analysis, we fitted the spectra using different combinations of these components. First, we used the `nthComp` model with seed photon temperature ($kT_{\rm seed}$) as a free parameter. Additionally, we tested combinations of the `nthComp` model with an additional soft thermal component (BB or MCD), where $kT_{\rm seed}$ was tied to the temperature of the thermal component, and the seed-photon shape parameter (`inp_Type`) was adjusted accordingly to the selected model.

For the BB model, we used the normalisation defined as $R^2_{\rm km}/D^2_{10}$ ($R_{\rm km}$ is the source radius in km and D_{10} is the distance to the source in units of 10 kpc) to determine the source radius. For the MCD model, we used the normalisation defined as $(R_{\rm in}/D_{10})^2 \cos\theta$ (where $R_{\rm in}$ is the apparent inner disc radius in km and θ is the inclination angle with respect to the observer, defined as $\theta = 0$ for face-on) to determine the apparent inner disc radius. For the MCD model we tested inclination angles of 40° and 70°, applied a correction factor for the torque-free inner boundary condition ($\xi = 0.4$) and the ratio of colour temperature to effective temperature ($\kappa = 1.7$; Kubota et al. 1998). The reported fluxes were calculated using the convolutional model `cflux`.

To assess the possible presence of the Fe Kα emission line at $\sim$ 6.4 keV, we performed over 10^5 spectral simulations in XSPEC to determine the significance level for detecting this feature. We used the observational dataset with the FAKEIT command and generated random parameters with the SIMPARS command. By constructing a cumulative distribution function of F-values from the simulations, we established the minimum significance level for detection by comparing the simulated F-values to the F-value from the data. We defined the null hypothesis as the continuum-only model (in XSPEC [CONST×TBABS×(NTHCOMP)]), while the tested hypothesis included both the continuum and the Gaussian component (GAUSS). We determined the significance level by calculating the associated p value, representing the fraction of simulated spectra with F-values greater than those obtained by fitting the real data. This simulation-based approach controls the false-positive rate when testing for an additional Gaussian component.

To account for *NuSTAR* calibration uncertainties (Madsen et al. 2015; Grefenstette et al. 2022; Madsen et al. 2022), we allowed the FPMA gain offset to vary while keeping the FPMB gain fixed. We obtained best-fitting offsets of −47 eV for SLX 1744-299 and −72 eV for SLX 1744-300, consistent with the typical ~40–80 eV systematic uncertainties reported in the literature (e.g. Zalot et al. 2024; Ballhausen et al. 2024; La Monaca et al. 2024; Diez et al. 2023).

We calculated the parameter errors at the 90 per cent confidence level using the Markov chain Monte Carlo technique implemented in XSPEC. We used the Goodman-Weare algorithm with a total of 10^7 steps, with walkers set to 10 times the number of free parameters (Goodman & Weare 2010). We verified convergence by inspecting the parameters' trace plots and by checking that the estimated autocorrelation times were stable (see Saavedra et al. 2023b,a for more details).

3. SLX 1744−299: Results

3.1. Time-averaged properties

Our detailed temporal analysis of SLX 1744−299 did not reveal any coherent signals, with a pulsed fraction upper limit of 3.9 per cent (90 per cent confidence), but the source exhibited significant aperiodic variability. From the 3–15 keV light curve, we measured a fractional rms variability of 23.2 ± 3.1 per cent (1σ), consistent with values typically observed in NS-LMXBs during the hard state (Muñoz-Darias et al. 2014), indicating that SLX 1744−299 was in this accretion regime during the *NuSTAR* observation.

We modelled the spectra using a standard approach for NS-LMXBs in the hard state. Our initial fit used a single thermally Comptonised continuum model affected by photoelectric absorption, assuming two scenarios: seed photons originating either from a BB or from a MCD (i.e. setting `inp_type` to 0 and 1, respectively). The two assumptions provided equally good statistical fits ($\chi^2_\nu = 1.04$ for 856 dof; p-value = 0.20), with no evident structured residuals across the energy range, including the Fe Kα region (Fig. 2, right panel). To quantify this, we tested for the presence of a narrow Fe emission line by adding a Gaussian component, but it was not significantly detected (2.1σ; see Sect. 2.2), and was therefore not included in any of the spectral models. For the BB scenario, we obtained $kT_{\rm seed} = 0.58 \pm 0.02$ keV; in the case of the MCD, we found $kT_{\rm seed} = 0.7 \pm 0.03$ keV. In both cases, we obtained a $\Gamma = 2.33 \pm 0.01$ and a $kT_e = 38^{+53}_{-12}$ keV. The unabsorbed 3–78 keV flux is $(1.77 \pm 0.01) \times 10^{-10}$ erg s^{-1} cm^{-2}, which corresponds to an upper limit on the luminosity of $(1.06 \pm 0.51) \times 10^{36}$ erg s^{-1}.

Adding a BB component (`bbodyrad`) to the model did not significantly improve the fit ($\Delta\chi^2 = 0.6$ for 1 dof; F-test probability of 0.47). The model parameters remained consistent with the previous fit, including the temperature of the BB component (which corresponds to the seed photon temperature, $kT_{\rm bb} = kT_{\rm seed}$). From the BB normalisation, we derived an emission radius of $R_{\rm bb} < 1.3$ km. In this model, the Comptonisation component accounts for > 98 per cent of the total 3–78 keV unabsorbed flux, while the thermal contribution is < 2 per cent. Table 1 presents the detailed results of the fitted models, and Fig. 2 (right panel) displays the corresponding spectrum and residuals.

We also tested a model consisting of an MCD plus Comptonisation. The fit returned parameters consistent with those from the single `nthComp` model (e.g. $kT_{\rm in} = 0.71 \pm 0.03$ keV). However, the corrected inner disc radius inferred from the `diskbb` normalisation ($N_{\rm diskbb} < 1.2 \times 10^{-5}$) corresponds to $R_{\rm in} < 3$ m, which is unphysically small compared to the typical NS radius of 10 km. Therefore, we discarded the model.

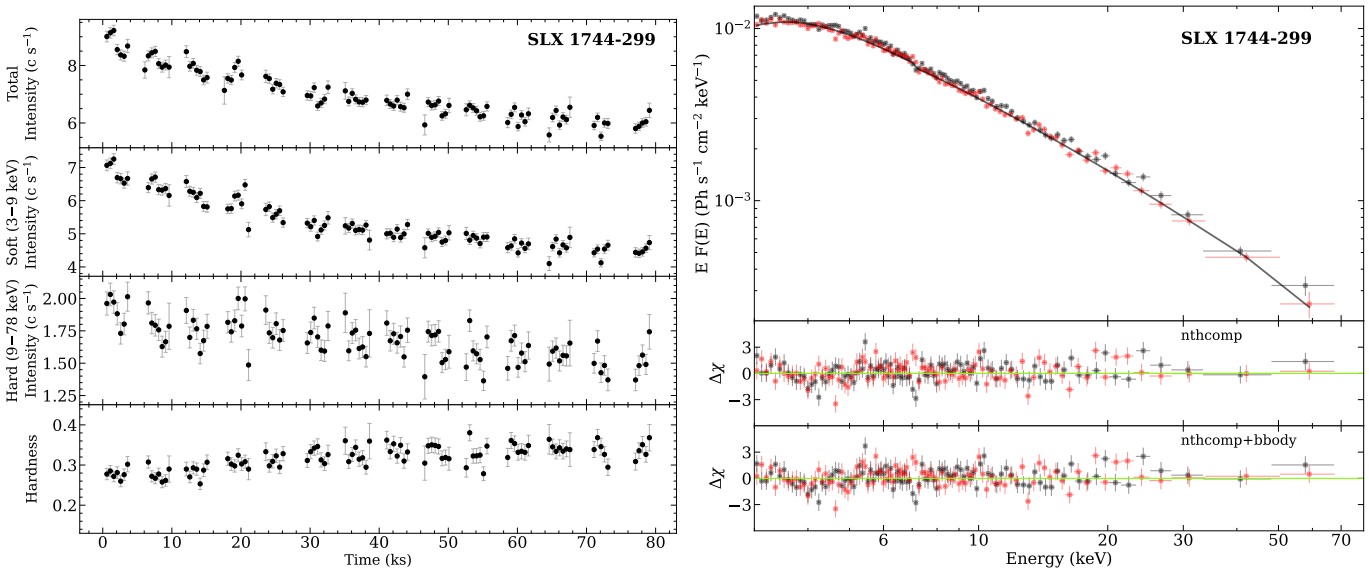


Fig. 2: *Left panel*: Background-corrected *NuSTAR* light curve of SLX 1744−299 with a time bin of 500 sec. From top to bottom: the total light curve in the 3–78 keV energy range, the soft band (3–9 keV), the hard band (9–78 keV), and the hardness ratio (hard-to-soft) as a function of time. *Right panel*: Unfolded *NuSTAR* FPMA (red) and FPMB (black) spectrum (top) and residuals (middle and bottom) using the `const×TBabs×(nthComp)` model. The bottom panel shows the fit residuals when using `const×TBabs×(bbodyrad+nthComp)`.

3.2. Time-resolved spectral analysis

The *NuSTAR* light curve of SLX 1744−299 (3–78 keV, 500 s bins) shows a gradual decline in count rate from 9.0 ± 0.2 to 6.4 ± 0.2 cts s^{-1}, corresponding to a 28 per cent decrease, over the 79 ks observation (see Fig. 2, top panel). When inspecting the light curve in different energy bands, the drop appears more pronounced in the soft range (3–9 keV), while the hard range (9–78 keV) remains relatively stable. Consequently, the hardness ratio increases from 0.28 ± 0.01 to 0.36 ± 0.02 during the first 40 ks.

In order to investigate the physical origin of this spectral evolution, we performed a time-resolved spectral analysis. We divided the observation into three consecutive 26 ks intervals and extracted one spectrum per segment. We fitted these three spectra using the preferred model identified for the entire observation (i.e., `const×TBabs×(nthComp)` with a BB geometry for the seed photons).

The model fitted all three intervals acceptably, yielding reduced chi-squared values (chi-squared and degrees of freedom) of 1.05 (733/692), 1.05 (721/686), and 1.01 (608/598), respectively. Our analysis revealed three key trends (see Fig. 3): first, a slight hardening of the photon index, which decreased from 2.47 ± 0.03 to 2.26 ± 0.03; second, a steady decline in the seed-photon temperature from 0.60 ± 0.02 keV to 0.21 ± 0.03 keV; and third, an increase in the electron temperature from 20^{+4}_{-2} keV to $\gtrsim 40$ keV (the latter being a lower limit).

This combination of a hardening photon index, a cooler seed photon temperature, and a hotter electron temperature is physically consistent with a declining mass-accretion rate ($\dot{M}$). This scenario suggests that the corona becomes less efficiently cooled as the observation progresses (see Sec. 5.2).

4. SLX 1744−300: Results

The *NuSTAR* light curve of SLX 1744−300 revealed two prominent Type-I bursts (see the top panel of Fig. 4). These events were excluded from the persistent emission analysis and are examined separately in Section 4.2. In the following, we first characterise the persistent emission and then analyse the bursts.

4.1. Persistent X-ray emission properties

We searched for periodic signals but found no significant periodicities, with a pulsed fraction upper limit of 9.1 per cent (90 per cent confidence). We determined the fractional rms variability to be 22.6 ± 4.3 per cent (1σ), which indicated that the source was in the hard state at the time of the observation (Muñoz-Darias et al. 2014).

We fitted the time-averaged spectra of the persistent emission with an absorbed thermal Comptonisation model. As in the case of SLX 1744−299 (Section 3), we considered two configurations for the seed photon source: the BB and the MCD. In both cases, the fits were statistically acceptable ($\chi^2_\nu = 1.03$ for 797 dof; p-value = 0.27). No significant Fe Kα emission line was detected (2.8σ; see Sect. 2.2). The BB scenario yielded a seed temperature $kT_{\rm seed} = 0.63 \pm 0.03$ keV, whereas the MCD case resulted in $kT_{\rm seed} = 0.76 \pm 0.04$ keV. The two assumptions returned consistent values for the photon index ($\Gamma = 2.28 \pm 0.02$) and the electron temperature ($kT_{\rm e} = 8.7 \pm 0.8$ keV). The unabsorbed 3–78 keV flux is $(2.02 \pm 0.01) \times 10^{-10}$ erg cm^{-2} s^{-1}, which corresponds to $L_{\rm X} < (2.56 \pm 0.43) \times 10^{36}$ erg s^{-1}.

Incorporating an additional `bbodyrad` component into the model did not significantly improve the fit ($\Delta\chi^2 = 0.8$ for 1 dof; F-test probability of 0.87). Using the normalisation from this component and adopting a distance of 10.3 ± 0.8 kpc, we estimated an upper limit of 1.2 km for the radius of this potential thermal emission region. Within this model, the Comptonisation component contributes > 99 per cent of the unabsorbed 3–78 keV flux, while the thermal fraction is < 1 per cent. Table 1 presents the detailed parameters, and Fig. 4 (right panel) illustrates the spectrum and model residuals.

Table 1: Best-fit spectral results for SLX 1744−299 and SLX 1744−300.

Component	Parameter	SLX 1744−299		SLX 1744−300	
		NTHCOMP	NTHCOMP+BBODYRAD	NTHCOMP	NTHCOMP+BBODYRAD
CONST	C_{AB}	1.03 ± 0.01	1.03 ± 0.01	1.03 ± 0.01	1.03 ± 0.01
TBABS	N_H (10^{22} cm^{-2})	$3.3^{\dagger}$	$3.3^{\dagger}$	$3.7^{\dagger}$	$3.7^{\dagger}$
NTHCOMP	Γ	2.33 ± 0.01	2.32 ± 0.01	2.28 ± 0.02	2.28 ± 0.02
	kT_e (keV)	38^{+53}_{-12}	37^{+19}_{-12}	8.7 ± 0.8	8.7 ± 0.5
	kT_{seed} (keV)	0.58 ± 0.02	$= kT_{bb}$	0.63 ± 0.03	$= kT_{bb}$
	$norm_{compt}$ ($\times 10^{-2}$)	1.3 ± 0.1	1.3 ± 0.1	1.4 ± 0.1	1.4 ± 0.1
BBODYRAD	kT_{bb} (keV)	-	0.57 ± 0.04	-	0.64 ± 0.03
	$norm_{bb}$	-	< 3.3	-	< 1.4
	R_{bb} [km] ^{b}	-	< 1.3	-	< 1.2
F_X^a [0.5–10 keV]		1.49 ± 0.01	1.54 ± 0.01	1.93 ± 0.01	1.93 ± 0.01
F_X^a [2–10 keV]		1.33 ± 0.01	1.36 ± 0.01	1.73 ± 0.01	1.73 ± 0.01
F_X^a [3–78 keV]		1.77 ± 0.01	1.77 ± 0.01	2.02 ± 0.01	2.02 ± 0.01
L_X^b [10^{36} erg s^{-1}]		$< 1.06 \pm 0.51$	$< 1.06 \pm 0.51$	$< 2.56 \pm 0.43$	$< 2.56 \pm 0.43$
χ^2_ν/dof		1.04/856	1.04/855	1.03/797	1.03/796

Notes. We used a thermal Comptonisation model, `const×TBabs×(nthComp)`, with `inp_Type = 0` and free kT_{seed}. We also used a combined model, `const×TBabs×(nthComp+bbodyrad)`, in which kT_{seed} is tied to the BB temperature (kT_{bb}). All parameter uncertainties are reported at the 90 per cent confidence level. † Corresponding parameter frozen during the fit. ^{a} Unabsorbed X-ray flux in units of 10^{-10} erg cm^{-2} s^{-1}. ^{b} Calculated in the 3–78 keV range, assuming an upper limit of 7.2 ± 1.4 kpc for SLX 1744−299 and 10.3 ± 0.8 kpc for SLX 1744−300.

Similarly to the case of SLX 1744−299, the MCD plus Comptonisation model produced unphysical results. This model returned a seed photon temperature $kT_{in} = 0.76 \pm 0.03$ keV. The corrected inner disc radius, which we inferred from the `diskbb` normalisation ($N_{diskbb} < 5.6 \times 10^{-5}$), was unphysically small ($R_{diskbb} < 11$ m for a 40° inclination and < 16 m for 70°). We therefore did not consider this model further.

4.2. Type-I thermonuclear burst properties

SLX 1744−300 exhibited two thermonuclear Type-I bursts during the *NuSTAR* observation. To characterise their temporal profiles, we fitted the burst profiles using the QDP BURS model[3]. This model represents each burst as a linear rise followed by an exponential decay, superimposed on a constant representing the persistent emission level. The model is defined as:

$$R(t) = \begin{cases} F_{pers} & t < t_{start} \\ F_{pers} + A \cdot \frac{(t - t_{start})}{t_{peak} - t_{start}} & t_{start} < t < t_{peak} \\ F_{pers} + A \cdot e^{-(t - t_{peak})/D_T} & t_{peak} < t, \end{cases} \quad (1)$$

where F_{pers} is the rate associated with the persistent emission. t_{start} and t_{peak} are the burst start time and peak time, respectively, indicating the onset and maximum intensity moments of the burst. The parameter A is the burst amplitude above the persistent level, and D_T is the decay time constant, which controls the rate at which the burst count rate decreases after its peak. The two bursts are shown at 1-s resolution in the insets of Fig. 4, together with the best-fit model from Eq. 1. We implemented a Monte Carlo sampling method to determine the 1σ uncertainties of the parameters, which are summarised in Table 2.

Burst-1 started at $30804.2^{+0.5}_{-0.1}$ s and lasted 34.2 ± 1.2 s. The rise time was $1.5^{+0.3}_{-0.6}$ s, and the decay time was 7.2 ± 0.3 s. The emission preceding Burst-1 was measured at 9.3 ± 0.8 cts s^{-1}, reaching a peak of 402.5 cts s^{-1}. Burst-2 started at $49033.2^{+0.4}_{-0.1}$ s and lasted 31.6 ± 1.4 s. The rise and decay times were $1.4^{+0.2}_{-0.5}$ s and 6.6 ± 0.3 s, respectively. The emission preceding Burst-2 was measured at 9.2 ± 0.7 cts s^{-1}, reaching a peak of 380.2 cts s^{-1}. The bursts are consistent with mixed H and He fuel (see Section 5.2.2).

To investigate the spectral evolution during these events, we also conducted a time-resolved spectroscopic study. We fitted the spectra from each burst using a fixed model for the persistent emission (i.e. a single thermal Comptonisation continuum), while allowing a soft thermal BB component to vary (e.g., in't Zand et al. 2011; Degenaar et al. 2016). By exploring different good time intervals, we achieved an optimal temporal resolution of six spectra per burst.

This analysis showed spectral cooling in both bursts. For burst-1, the thermal temperature cooled from 2.61 ± 0.35 to 1.42 ± 0.21 keV, while the apparent emission radius inferred

[3] See https://heasarc.gsfc.nasa.gov/docs/software/ftools/others/qdp/node143.html

Table 2: Best-fit burst parameters.

Burst No	Burst start time (s)	Burst duration (s)	Rise time (s)	Decay time (s)	Persistent emission (cts s^{-1})	Peak count rate (cts s^{-1})
1	$30804.2^{+0.5}_{-0.1}$	34.2 ± 1.2	$1.5^{+0.3}_{-0.6}$	7.2 ± 0.3	9.3 ± 0.8	402.5
2	$49033.2^{+0.4}_{-0.1}$	31.6 ± 1.4	$1.4^{+0.2}_{-0.5}$	6.6 ± 0.3	9.2 ± 0.7	380.2

Notes. The two type-I X-ray bursts were modelled with the BURS model. Uncertainties correspond to 1σ.

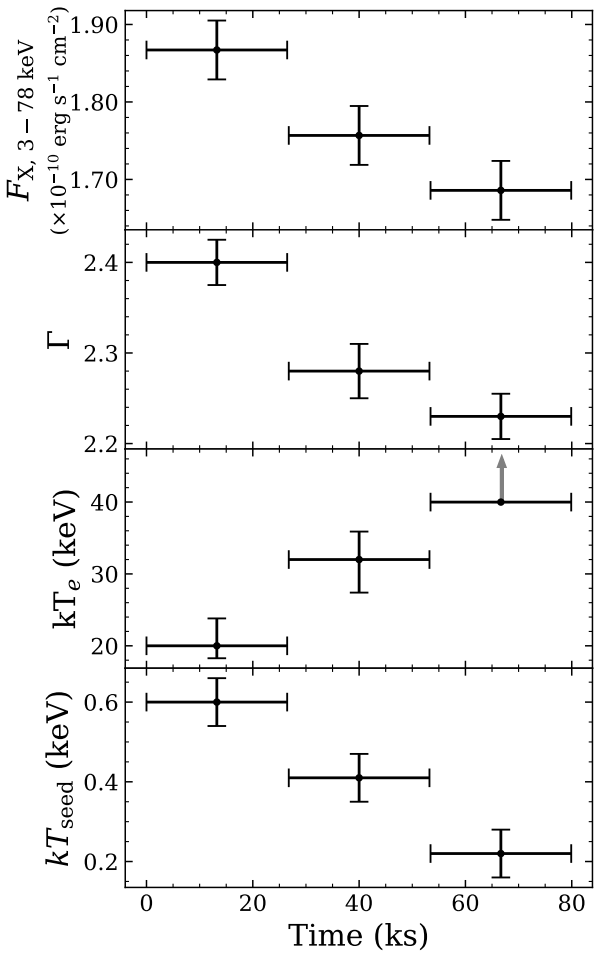


Fig. 3: Time-resolved spectral evolution of SLX 1744−299. From top to bottom: unabsorbed 3–78 keV X-ray flux, photon index (Γ), electron temperature (kT_e), and seed-photon temperature (kT_{seed}). Error bars represent 90 per cent confidence intervals.

from the BB normalisation increased from $3.1^{+1.4}_{-0.9}$ to $6.1^{+2.0}_{-1.6}$ km, assuming $d = 10.3$ kpc. For burst-2, the temperature cooled from 1.85 ± 0.24 to 0.98 ± 0.15 keV, while the apparent radius increased from $4.1^{+1.3}_{-1.1}$ to $7.7^{+4.2}_{-2.8}$ km. The corresponding bolometric burst fluences (f_b), derived from the time-resolved unabsorbed 0.01–100 keV fluxes, were $(6.4 \pm 0.4) \times 10^{-8}$ erg cm^{-2} and $(5.1 \pm 0.4) \times 10^{-8}$ erg cm^{-2} for the first and second bursts, respectively. We found no evidence of photospheric radius expansion in either event, which prevented us from further constraining the source distance.

5. Discussion

Low-mass X-ray binaries at X-ray luminosities $\lesssim 0.01 L_{Edd}$ provide crucial insights into accretion physics, although their study is often limited by observational constraints. The two LMXBs, SLX 1744−299 and SLX 1744−300 offer an excellent opportunity to probe this low-luminosity regime, as they are persistent systems accreting at $\lesssim 0.01\ L_{Edd}$. However, their small angular separation has historically made it difficult to disentangle their individual contributions. For the first time above 10 keV, the exceptional spatial resolution and broad 3–78 keV energy coverage of *NuSTAR* allowed us to carry out a detailed spectral and timing study of these two sources.

5.1. The low-luminosity hard state

From the *NuSTAR* observation, we were able, for the first time, to measure the integrated fractional rms (0.1–64 Hz) for SLX 1744−299 and SLX 1744−300 individually. We obtained values of ∼ 21—23 per cent in both cases, consistent with the sources being in the hard state during the observation (Muñoz-Darias et al. 2014). The spectral analysis of the systems is consistent with the above picture. The X-ray spectra of both sources are well described by a simple absorbed thermally Comptonised model.

The spectral fitting returned similar values of the photon indices (Γ ∼ 2.3) and seed photon temperatures ($kT_{seed} \sim 0.6$ keV), assuming the seed photons arise from the NS surface or boundary layer. However, the electron temperature of the Comptonising corona differed between the two sources: for SLX 1744−299 we found $kT_e \approx 38$ keV, while for SLX 1744−300 it was $kT_e \approx 9$ keV. These Γ and kT_e values translated to an optical depth[4] of $\tau \approx 1.5$ and ≈ 4.4 for SLX 1744−299 and SLX 1744−300, respectively. During hard state, NS-LMXBs show higher electron temperatures ($kT_e \gtrsim 10$ keV) and lower optical depths ($\tau \lesssim 3$) than in the soft state (where $kT_e \lesssim 5$ keV and $\tau \gtrsim 5$ is typically found; see e.g. Lin et al. 2007; Armas Padilla et al. 2017; Burke et al. 2017). Hence, SLX 1744−299 is fully consistent with typical hard state values while SLX 1744−300 shows a slightly higher τ than typical.

To test whether the thermal emission originates from the NS surface or boundary layer, or from the inner disc, we added either BB or MCD components to the Comptonisation model. We

[4]The electron scattering optical depth (τ) is obtained following the relation $\Gamma_\tau = [9/4 + ((kT_e/m_e c^2)\,\tau\,(1+\tau/3))^{-1}]^{1/2} - 1/2$.

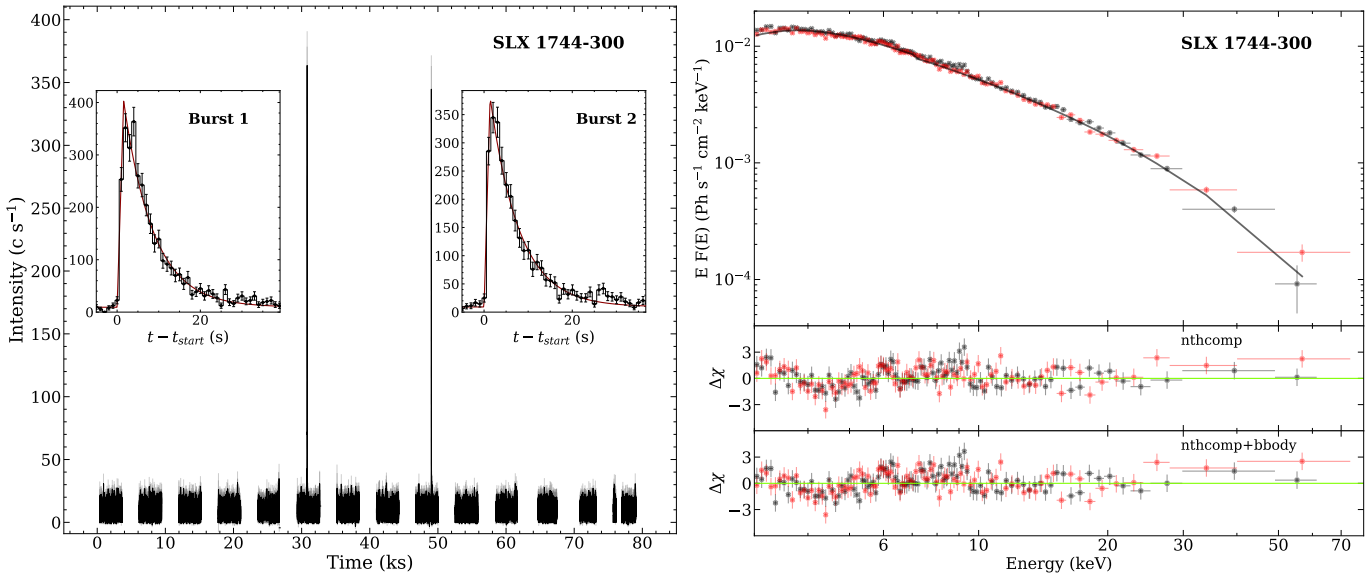


Fig. 4: *Left panel*: Background-corrected *NuSTAR* light curve of SLX 1744−300 with a time bin of 1 s, including two Type-I bursts superimposed on the persistent emission. The insets show each burst and the best-fit model from Eq. 1. *Right panel*: Unfolded *NuSTAR* FPMA (red) and FPMB (black) spectrum (top) and residuals (middle) using the `const×TBabs×(nthComp)` model. The bottom panel shows the fit residuals when using `const×TBabs×(bbodyrad+nthComp)`.

found that the data (i.e. the *NuSTAR* band) did not statistically require any additional thermal component. Including a BB model, the parameters of the Comptonisation component remained unchanged. The BB temperature was consistent with the previous seed photon temperature ($kT_{\rm bb} \approx 0.6$ keV), and the component contributed approximately < 2 per cent and < 1 per cent to the 3–78 keV flux for SLX 1744−299 and SLX 1744−300, respectively. When we replaced the BB with a MCD model, the fit returned unphysically small inner-disc radii.

We note that the *NuSTAR* spectral coverage starts at 3 keV and thus offers limited sensitivity to very soft thermal emission below that threshold. Nonetheless, the absence of a significant soft component in our spectra is consistent with established luminosity-dependent trends for NS-LMXBs: soft thermal components typically contribute ∼30–50 per cent of the 0.5–10 keV emission at low luminosities $L_{0.5-10} \lesssim 10^{35}$ erg s^{-1} (∼ 20 per cent in the 0.8–30 keV band), attributed to residual accretion on the NS surface (Zampieri et al. 1995; Armas Padilla et al. 2013b; Bahramian et al. 2017; Degenaar et al. 2013; Armas Padilla et al. 2013a; Arnason et al. 2015; Armas Padilla et al. 2018, 2017). Above 10^{35} erg s^{-1}, however, this component weakens or, in some cases, disappears (Armas Padilla et al. 2013a; Allen et al. 2015; Wijnands et al. 2015; Stoop et al. 2021). In this context, several broad-band studies have shown that the dominant component is thermal Comptonisation: the soft thermal component typically contributes only ≲ 10–20 per cent at energies up to ∼ 80 keV, while the Comptonised continuum carries most of the broad-band emission (e.g. Degenaar et al. 2015; Matranga et al. 2017; Ludlam et al. 2017; van den Eijnden et al. 2018). Therefore, our estimated luminosities ($L_{\rm X} \lesssim 1.06 \times 10^{36}$ erg s^{-1} for SLX 1744−299 and $L_{\rm X} \lesssim 2.56{\times}10^{36}$ erg s^{-1} for SLX 1744−300) are consistent with hard-state NS-LMXBs in which any soft thermal component contributes only a minor fraction of the 3–78 keV flux and remains undetectable in the *NuSTAR* band.

5.2. Variability across different timescales

The small angular separation between SLX 1744−300 and SLX 1744−299 (∼ 2.7 arcmin) has long hindered efforts to measure their individual X-ray flux contributions. This limitation was first overcome by Mori et al. (2005), who used an *XMM-Newton* observation to spatially resolve the two sources and report their respective 0.5–10 keV fluxes. In that work, the absorbed 0.5–10 keV flux of SLX 1744−299 was reported to be higher than that of SLX 1744−300 by a factor of 1.9, with measured absorbed fluxes of 1.9×10^{-10} erg cm^{-2} s^{-1} and 1.0×10^{-10} erg cm^{-2} s^{-1}, respectively. In contrast, our *NuSTAR* observation provides, for the first time above 10 keV, spatially resolved flux measurements over the 3–78 keV energy band. We measured unabsorbed fluxes of 1.8×10^{-10} erg cm^{-2} s^{-1} and 2×10^{-10} erg cm^{-2} s^{-1} for SLX 1744−299 and SLX 1744−300, respectively, implying that SLX 1744−300 is now slightly brighter, with a flux ratio of ∼ 1.15 (∼ 1.3 when extrapolated to the 0.5–10 keV band). We note that long-term monitoring of the field by the *Rossi X-ray Timing Explorer* (in't Zand et al. 2007) also showed significant variability. In addition, our observations show variability on timescales of a few tens of kiloseconds. All the above suggests that the flux ratio between the two sources is not fixed and that it changes across short and long timescales.

5.2.1. SLX 1744−299

We performed time-resolved spectroscopy on SLX 1744−299 to trace its spectral evolution throughout the observation. Our analysis revealed a gradual flux decline of 28 per cent over the 79 ks exposure. As the flux decreased, the spectrum hardened: the photon index decreased from ∼ 2.4 to ∼ 2.2, the seed-photon temperature cooled from ∼ 0.6 to ∼ 0.2 keV, and the coronal temperature rose from ∼ 20 to ≳ 40 keV. This spectral evolution is consistent with a decreasing mass-accretion rate. A lower accretion rate supplied fewer seed photons from the boundary layer or the inner accretion disc, making inverse-Compton cooling less efficient. This reduced cooling allowed the coronal electrons to

heat up, increasing kT_e and hardening the emitted spectrum – naturally explaining the observed evolution (see e.g. Done et al. 2007).

This steady decrease in source intensity is reminiscent of the behaviour observed in other NS-LMXBs. In particular, similar trends have been reported for the transient UCXB IGR J17494−3030 (Armas Padilla et al. 2013b) and the UCXB candidate XTE J1709−267 (Degenaar et al. 2013). In both systems, *XMM-Newton* observations revealed a comparable decline in flux at $L_X < 10^{35}$ erg s^{-1}. However, unlike our case, time-resolved spectroscopy showed that the decrease in intensity was accompanied by a drop in the inferred temperature of the thermal component, while the photon index (Γ) remained constant. In those works, the flux decay was interpreted as the result of decreasing low-level accretion onto the NS surface, which produced the observed soft thermal emission (we note that although crustal cooling was initially suggested for XTE J1709−267, it was later disfavoured; Armas Padilla et al. 2013b).

In our case, the *NuSTAR* low-energy limit (3 keV) prevents us from constraining the soft thermal component, and therefore from confirming or ruling out whether a similar trend is taking place. Still, we observe a decrease in the seed photon temperature, which we assume originates from the NS surface, suggesting a potentially analogous scenario. However, we also detect a clear spectral evolution in the Comptonisation component, including an increase in the electron temperature and a hardening of the photon index. These results suggest an overall spectral evolution, encompassing both seed photon and Comptonisation properties, suggesting that the fading was driven by changes in the accretion rate. We note that it is also possible that a similar evolution in the Comptonisation component took place in the aforementioned cases of IGR J17494−3030 and XTE J1709−267. However, this could not be properly characterised in those studies due to the limited energy coverage of the *XMM-Newton* observations, which made the hard X-ray spectral shape more difficult to constrain.

5.2.2. SLX 1744−300

The system exhibited two Type-I X-ray bursts. Both events had durations of about 30 s and displayed clear spectral softening, with the BB temperature decreasing from ∼ 2 keV to ∼ 0.7 keV during the decay, as typically observed during the cooling phase of the NS photosphere following thermonuclear ignition (see e.g. Lewin et al. 1993). The burst fluences were of the order of $f_b = 5{-}7{\times}10^{-8}$ erg cm^{-2}. We found no evidence of photospheric radius expansion in either burst, consistent with previous observations (Chelovekov et al. 2017).

The detection of two bursts establishes an upper limit on the recurrence time of $\tau_{rec} \lesssim 5$ h during this epoch, refining the previous constraint of < 7.4 h reported by Chelovekov et al. (2017). We note that additional bursts may have gone undetected during data gaps caused by Earth occultations. The estimation of the recurrence time helps constrain the burning regime, and thus the fuel composition. The time typically required to exhaust accreted hydrogen via stable burning is $t_H \approx 11\,\mathrm{h}\left(\frac{0.02}{Z_{CNO}}\right)\left(\frac{X}{0.7}\right)$, where Z_{CNO} is the CNO mass fraction and X the hydrogen mass fraction. For solar-type metallicities, our derived $\tau_{rec} \lesssim 5$ h is significantly shorter than t_H, implying that a substantial fraction of hydrogen remains at the onset of the thermonuclear runaway. This favours mixed H/He burning (see, e.g., Cumming 2004).In this case, we can adopt a representative value of $\alpha \sim 40$, typically observed in mixed H/He bursts (Galloway et al. 2008), to obtain an order-of-magnitude estimate of the persistent bolometric flux. The α parameter is defined as the ratio between the accretion fluence accumulated between bursts and the burst fluence itself ($\alpha = F_{pers}\Delta t / f_b$; Lewin et al. 1993). Using the measured bolometric burst fluences together with the observed recurrence time between the two bursts ($\Delta t \simeq 1.82 \times 10^4$ s), we infer a bolometric persistent flux of $\sim (1.1 - 1.4) \times 10^{-10}$ erg cm^{-2} s^{-1}. Assuming the distance upper limit of $d < 10.3$ kpc, this corresponds to $L_{pers} \lesssim 1.8 \times 10^{36}$ erg s^{-1}, in good agreement with the luminosity independently inferred from the spectral fits to the persistent emission.

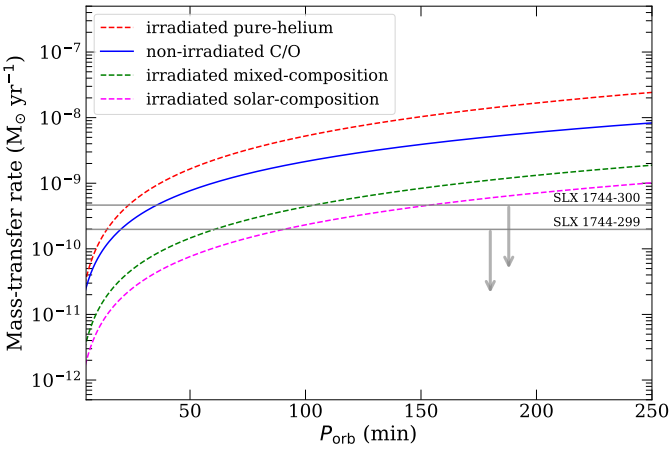


Fig. 5: Stability limits for non-irradiated C/O discs, irradiated mixed-composition discs and irradiated solar-composition discs based on Menou et al. (2002) and Lasota et al. (2008). In both cases, the upper limits on the mass transfer rate reported in this work yield upper limits on P_{orb}.

5.3. Thermal–viscous stability constraints on the P_{orb} limits

One of the few indirect diagnostics available to identify UCXB candidates in the absence of direct P_{orb} measurements is their persistent behaviour at low accretion rates. According to the DIM (Lasota 2001; see also Coriat et al. 2012), systems accreting at very low rates should be transient unless they have very short orbital periods, even within the ultracompact regime. This would allow their discs to remain fully ionised (i.e. thermally stable) even at low $\dot{M}$ (in't Zand et al. 2007). To investigate whether this could be the case for SLX 1744−299 and SLX 1744−300, we estimated their mass accretion rates ($\dot{M}_{acc}$) from their observed persistent X-ray luminosities using $L_X = \eta c^2 \dot{M}_{acc}$ and assuming a radiatively efficient scenario (i.e. $\eta = 0.1$; e.g. Coriat et al. 2012). These values were then compared with the critical stability thresholds predicted by DIM, in which thermal–viscous stability is governed by the mass-transfer rate from the donor star (assuming $\dot{M}_{transfer} \simeq \dot{M}_{acc}$) and the orbital period (P_{orb}).

For SLX 1744−299, the persistently faint X-ray luminosity of $L_X \lesssim 1.06 \times 10^{36}$ erg s^{-1} implies $\dot{M}_{acc} \lesssim 1.9 \times 10^{-10} M_\odot$ yr^{-1}. Comparing the inferred $\dot{M}_{acc}$ with the critical stability thresholds predicted by the DIM, we find that a persistently stable disc at this accretion rate requires an orbital period $P_{orb} \lesssim 90$ min, indicating that an ultracompact nature is a highly plausible scenario (see Fig. 5). In fact, this low accretion rate, together with the detection of slow-recurrence, intermediate-duration bursts, had already led to the source being proposed as a UCXB candidate

and included in catalogues of such systems (in't Zand et al. 2007; Armas Padilla et al. 2023).

For SLX 1744−300, we inferred an X-ray luminosity of $L_X \lesssim 2.56 \times 10^{36}$ erg s^{-1}, corresponding to $\dot{M}_{acc} \lesssim 4.5 \times 10^{-10}$ $M_\odot$ yr^{-1} and $P_{orb} \lesssim 155$ min. This constraint on P_{orb} is therefore compatible with a short-period LMXB, including a UCXB. As a matter of fact, if the actual distance were $\lesssim 6.5$ kpc, the inferred mass accretion rate would lie just above the instability threshold for such systems (i.e. $P_{orb} < 80$ min). However, given that P_{orb} values above this threshold are allowed, and considering the properties of the short burst (Sec. 5.2.2) detected in this source, we note that SLX 1744−300 is a significantly weaker UCXB candidate than SLX 1744−299.

The UCXB interpretation can also be compared with the homogeneous *NuSTAR* study of confirmed UCXBs by Borghese et al. (2026). In that work, hard-state UCXBs, with luminosities in the $\sim 10^{35} - 10^{37}$ erg s^{-1} range, were generally described with two- or three-component models including one or two thermal components associated with the NS surface or boundary layer, the accretion disc, or both, together with a dominant Comptonised continuum. These systems displayed BB temperatures of $kT_{BB} \sim 0.5 - 1.5$ keV, disc temperatures of $kT_{disc} \sim 0.4 - 0.8$ keV, electron temperatures of $kT_e \sim 10 - 40$ keV, and photon indices of $\Gamma \sim 1.8 - 2.0$. Both SLX 1744−299 and SLX 1744−300 broadly fall within the above ranges, although their photon indices ($\Gamma \sim 2.3$) are somewhat softer than the average values found in that sample. In particular, the coronal temperature derived for SLX 1744−299 ($kT_e \sim 38$ keV) lies well within the range observed in hard-state UCXBs, while SLX 1744−300 ($kT_e \sim 9$ keV) lies at the lower end of the distribution.

A notable difference, however, is that our *NuSTAR* spectra do not statistically require additional thermal components, and any such contribution remains minimal when included. In the homogeneous UCXB study by Borghese et al. (2026), only two sources, IGR J17494–3030 and 47 Tuc X–9, did not require thermal components. This may be related to their significantly lower luminosities of $\sim 10^{34} - 10^{35}$ erg s^{-1}, although poorer counting statistics may also play a role. In this context, the absence of a thermal component in our spectra could also indicate luminosities closer to the $\sim 10^{35}$ erg s^{-1} regime, which would be possible if the distances to SLX 1744−299 and SLX 1744−300 are significantly below the current upper limits. Overall, the comparison remains compatible with a UCXB interpretation for both systems, although the case appears stronger for SLX 1744−299.

6. Conclusion

We analysed a *NuSTAR* observation, which enabled us to separate the contributions of the NS-LMXBs SLX 1744−299 and SLX 1744−300 (located only ∼2.7 arcmin apart) in the hard energy band for the first time. We find SLX 1744−300 to be slightly brighter, with a flux ratio of ~ 1.15 in the 3–78 keV band (~ 1.3 when extrapolated to the 0.5–10 keV band). The average spectra of both sources are well described by a thermally Comptonised model, which returned spectral parameters consistent with those of NS-LMXBs during the low-luminosity hard state. This is in agreement with the high fractional rms values (∼21–23 per cent) measured in both cases. The evolution of both sources throughout the ~ 80 ks covered by the observation was markedly different. While SLX 1744−299 showed a constant decrease in flux, likely due to variations in the mass-accretion rate, SLX 1744−300 remained steady but exhibited two short Type I bursts consistent with mixed hydrogen/helium burning.

These observations, combined with previously reported upper limits on the distance, yield low persistent X-ray luminosities of $L_X \lesssim 1.1 \times 10^{36}$ erg s^{-1} and $L_X \lesssim 2.6 \times 10^{36}$ erg s^{-1} for SLX 1744−299 and SLX 1744−300, respectively. By comparing the inferred mass-accretion rates (from these luminosities) with the critical values for disc stability predicted by the DIM, we found $P_{orb} \lesssim 90$ min and $P_{orb} \lesssim 105$–155 min. While both constraints are technically compatible with the UCXB regime, the former case (i.e. SLX 1744−299) is significantly more robust, not only based on these values but also in light of the intermediate-duration burst previously reported for this source.

Acknowledgements. We thank the anonymous referee for their careful reading of the manuscript and for their comments, which helped improve the clarity of the paper. We acknowledge support by Spanish Agencia estatal de investigación via PID2021-124879NB-I00 and PID2024-161863NB-I00. M.A.P. acknowledges support through the Ramón y Cajal grant RYC2022-035388-I, funded by MCIU/AEI/10.13039/501100011033 and FSE+.

References

Alizai, K., Chenevez, J., Brandt, S., & Lund, N. 2020, MNRAS, 494, 2509
Allen, J. L., Linares, M., Homan, J., & Chakrabarty, D. 2015, ApJ, 801, 10
Amaro-Seoane, P., Andrews, J., Arca Sedda, M., et al. 2023, Living Reviews in Relativity, 26, 2
Armas Padilla, M., Corral-Santana, J. M., Borghese, A., et al. 2023, A&A, 677, A186
Armas Padilla, M., Degenaar, N., & Wijnands, R. 2013a, MNRAS, 434, 1586
Armas Padilla, M., Ponti, G., De Marco, B., Muñoz-Darias, T., & Haberl, F. 2018, MNRAS, 473, 3789
Armas Padilla, M., Ueda, Y., Hori, T., Shidatsu, M., & Muñoz-Darias, T. 2017, MNRAS, 467, 290
Armas Padilla, M., Wijnands, R., & Degenaar, N. 2013b, MNRAS, 436, L89
Arnason, R. M., Sivakoff, G. R., Heinke, C. O., Cohn, H. N., & Lugger, P. M. 2015, ApJ, 807, 52
Arnaud, K. A. 1996, in Astronomical Society of the Pacific Conference Series, Vol. 101, Astronomical Data Analysis Software and Systems V, ed. G. H. Jacoby & J. Barnes, 17
Bachetti, M. 2018, HENDRICS: High ENergy Data Reduction Interface from the Command Shell, Astrophysics Source Code Library, record ascl:1805.019
Bachetti, M. & Huppenkothen, D. 2018, ApJ, 853, L21
Bahramian, A. & Degenaar, N. 2023, in Handbook of X-ray and Gamma-ray Astrophysics. Edited by Cosimo Bambi and Andrea Santangelo, 120
Bahramian, A., Heinke, C. O., Tudor, V., et al. 2017, MNRAS, 467, 2199
Ballhausen, R., Thalhammer, P., Pradhan, P., et al. 2024, A&A, 688, A214
Blackburn, J. K. 1995, in Astronomical Society of the Pacific Conference Series, Vol. 77, Astronomical Data Analysis Software and Systems IV, ed. R. A. Shaw, H. E. Payne, & J. J. E. Hayes, 367
Borghese, A., Armas Padilla, M., & Muñoz-Darias, T. 2026, AA, 710, A43
Burke, M. J., Gilfanov, M., & Sunyaev, R. 2017, MNRAS, 466, 194
Chelovekov, I. V., Grebenev, S. A., Mereminskiy, I. A., & Prosvetov, A. V. 2017, Astronomy Letters, 43, 781
Chen, H.-L., Tauris, T. M., Han, Z., & Chen, X. 2021, MNRAS, 503, 3540
Coriat, M., Fender, R. P., & Dubus, G. 2012, MNRAS, 424, 1991
Cruz-Sanchez, N., Saavedra, E. A., Fogantini, F. A., García, F., & Combi, J. A. 2026a, A&A, 705, A136
Cruz-Sanchez, N., Saavedra, E. A., Fogantini, F. A., et al. 2026b, A&A, 707, L20
Cumming, A. 2004, Nuclear Physics B Proceedings Supplements, 132, 435
Degenaar, N., Koljonen, K. I. I., Chakrabarty, D., et al. 2016, MNRAS, 456, 4256
Degenaar, N., Miller, J. M., Chakrabarty, D., et al. 2015, MNRAS, 451, L85
Degenaar, N., Wijnands, R., & Miller, J. M. 2013, ApJ, 767, L31
Diez, C. M., Grinberg, V., Fürst, F., et al. 2023, A&A, 674, A147
Done, C., Gierliński, M., & Kubota, A. 2007, A&A Rev., 15, 1
Fortin, F., Kalsi, A., García, F., Simaz-Bunzel, A., & Chaty, S. 2024, AA, 684, A124
Galloway, D. K., Muno, M. P., Hartman, J. M., Psaltis, D., & Chakrabarty, D. 2008, ApJS, 179, 360
Goodman, J. & Weare, J. 2010, Communications in Applied Mathematics and Computational Science, 5, 65
Grefenstette, B., Brightman, M., Earnshaw, H. P., et al. 2022, arXiv e-prints, arXiv:2206.04058
Harrison, F. A., Craig, W. W., Christensen, F. E., et al. 2013, ApJ, 770, 103
Huppenkothen, D., Bachetti, M., Stevens, A. L., et al. 2019, ApJ, 881, 39

in't Zand, J. J. M., Galloway, D. K., & Ballantyne, D. R. 2011, A&A, 525, A111
in't Zand, J. J. M., Jonker, P. G., & Markwardt, C. B. 2007, A&A, 465, 953
Kawai, N., Fenimore, E. E., Middleditch, J., et al. 1988, ApJ, 330, 130
Koglin, J. E., An, H., Barrière, N., et al. 2011, in Society of Photo-Optical Instrumentation Engineers (SPIE) Conference Series, Vol. 8147, Society of Photo-Optical Instrumentation Engineers (SPIE) Conference Series, ed. S. L. O'Dell & G. Pareschi, 81470J
Kubota, A., Tanaka, Y., Makishima, K., et al. 1998, PASJ, 50, 667
La Monaca, F., Di Marco, A., Poutanen, J., et al. 2024, ApJ, 960, L11
Lasota, J.-P. 2001, New A Rev., 45, 449
Lasota, J. P., Dubus, G., & Kruk, K. 2008, A&A, 486, 523
Lewin, W. H. G., van Paradijs, J., & Taam, R. E. 1993, Space Sci. Rev., 62, 223
Lin, D., Remillard, R. A., & Homan, J. 2007, ApJ, 667, 1073
Ludlam, R. M., Miller, J. M., Bachetti, M., et al. 2017, ApJ, 836, 140
Madsen, K. K., Forster, K., Grefenstette, B., Harrison, F. A., & Miyasaka, H. 2022, Journal of Astronomical Telescopes, Instruments, and Systems, 8, 034003
Madsen, K. K., Grefenstette, B. W., Pike, S., et al. 2020, arXiv e-prints, arXiv:2005.00569
Madsen, K. K., Harrison, F. A., Markwardt, C. B., et al. 2015, ApJS, 220, 8
Makishima, K., Maejima, Y., Mitsuda, K., et al. 1986, ApJ, 308, 635
Matranga, M., Papitto, A., Di Salvo, T., et al. 2017, A&A, 603, A39
Menou, K., Perna, R., & Hernquist, L. 2002, ApJ, 564, L81
Mitsuda, K., Inoue, H., Koyama, K., et al. 1984, PASJ, 36, 741
Mori, H., Maeda, Y., Pavlov, G. G., Sakano, M., & Tsuboi, Y. 2005, Advances in Space Research, 35, 1137
Muñoz-Darias, T., Fender, R. P., Motta, S. E., & Belloni, T. M. 2014, MNRAS, 443, 3270
Muñoz-Darias, T., Motta, S., & Belloni, T. M. 2011, MNRAS, 410, 679
Nelemans, G. 2018, arXiv e-prints, arXiv:1807.01060
Nelemans, G. & Jonker, P. G. 2010, New A Rev., 54, 87
Paczynski, B. & Sienkiewicz, R. 1981, ApJ, 248, L27
Pavlinsky, M., Tkachenko, A., Levin, V., et al. 2021, A&A, 650, A42
Pavlinsky, M. N., Grebenev, S. A., & Sunyaev, R. A. 1994, ApJ, 425, 110
Rappaport, S., Joss, P. C., & Webbink, R. F. 1982, ApJ, 254, 616
Saavedra, E. A., Fogantini, F. A., Escobar, G. J., et al. 2023a, A&A, 680, A88
Saavedra, E. A., García, F., Fogantini, F. A., et al. 2023b, MNRAS, 522, 3367
Skinner, G. K., Foster, A. J., Willmore, A. P., & Eyles, C. J. 1990, MNRAS, 243, 72
Skinner, G. K., Willmore, A. P., Eyles, C. J., Bertram, D., & Church, M. J. 1987, Nature, 330, 544
Stoop, M., van den Eijnden, J., Degenaar, N., et al. 2021, MNRAS, 507, 330
Tauris, T. M. 2018, Phys. Rev. Lett., 121, 131105
van den Eijnden, J., Degenaar, N., Pinto, C., et al. 2018, MNRAS, 475, 2027
van Haaften, L. M., Nelemans, G., Voss, R., et al. 2013, A&A, 552, A69
Verbunt, F. & van den Heuvel, E. P. J. 1995, in X-ray Binaries, 457–494
Verner, D. A., Ferland, G. J., Korista, K. T., & Yakovlev, D. G. 1996, ApJ, 465, 487
Wijnands, R., Degenaar, N., Armas Padilla, M., et al. 2015, MNRAS, 454, 1371
Wilms, J., Allen, A., & McCray, R. 2000, ApJ, 542, 914
Zalot, N., Sokolova-Lapa, E., Stierhof, J., et al. 2024, A&A, 686, A95
Zampieri, L., Turolla, R., Zane, S., & Treves, A. 1995, ApJ, 439, 849
Zdziarski, A. A., Johnson, W. N., & Magdziarz, P. 1996, MNRAS, 283, 193
Zhu, C.-H., Lü, G.-L., & Wang, Z.-J. 2012, Research in Astronomy and Astrophysics, 12, 1526
Życki, P. T., Done, C., & Smith, D. A. 1999, MNRAS, 309, 561